Solid State Phenomena
ISSN: 1662-9779, Vol. 376, pp 1-9
doi:10.4028/p-1KnpOd

Submitted: 2024-09-20
Revised: 2025-08-02
Accepted: 2025-08-04
Online: 2025-09-10

Punching of Prismatic Dislocation Loops from Inclusions in 4H-SiC Wafers

Qianyu Cheng[1,a*], Kevin Kayang[1,b], Zeyu Chen[1,c], Shanshan Hu[1,d], Balaji Raghothamachar[1,e], Michael Dudley[1,f], Dilip Gersappe[1,g], Andrey Soukhojak[2,h], Sungchul Baek[2,i]

[1]Department of Materials Science & Chemical Engineering, Stony Brook University, Stony Brook, NY 11794 U.S.A.

[2]SK siltron css, 5300 11 Mile Road, Bay City, MI 48611 U.S.A.

[a]qycheng96@hotmail.com, [b]kevin.kayang@stonybrook.edu, [c]zeyu.chen@stonybrook.edu, [d]shanshan.hu@stonybrook.edu, [e]balaji.raghothamachar@stonybrook.edu, [f]michael.dudley@stonybrook.edu, [g]dilip.gersappe@stonybrook.edu, [h]andrey.soukhojak@sksiltron.com, [i]sungchul.baek@sksiltron.com

Keywords: prismatic punched dislocation loop, inclusion, array of TED pairs, crystal growth.

Abstract. Indentation behavior induced by the presence of foreign inclusions in a PVT-grown 4H-SiC wafer is investigated through synchrotron X-ray topography, which revealed the generation of dislocation arrays from the inclusion center along six $\langle 11\bar{2}0 \rangle$ directions. Grazing-incident topographs shows these dislocation arrays exhibit contrast configurations of opposite-signed TED pairs or BPD segments. This correlates with dislocation loops generated due to prismatic punching, and dislocation configuration variation is dependent on the position of prismatic loops with respect to the wafer surface. The stress induced by the inclusion embedded in the 4H-SiC matrix is estimated from the difference in the thermomechanical properties, as the crystal is cooled from the growth temperature.

Introduction

Silicon carbide (SiC) is a wide bandgap semiconducting material that has gained significant attention owing to its exceptional electronic and physical properties, including high saturation velocity, high breakdown field, and excellent thermal conductivity. These attributes make SiC highly suitable for applications in power electronics, high-frequency devices, and harsh environments. As SiC is steadily replacing the traditional silicon devices in industries that require high-efficiency, high-power, and high-temperature operation, understanding and advancing SiC crystal growth with high quality is crucial for developing devices that meet the requirements of these advanced applications.

Prismatic punching can be induced through the formation and emission of dislocation loops of prismatic nature when a small particle with a strong contrast of thermomechanical properties vs. the host crystal forms an inclusion in the latter. The system behaves as an indentation punch that pushes prisms of the host crystal in the prismatic axis direction. The slip planes bounding the prism surface are displaced by the indenter with shearing stress, which can generate rings of dislocations through the Frank-Read mechanism [1-5]. Such prismatic punched dislocation loops were first discussed by Seitz in thallous halide crystals [1] and observed by Jones and Mitchell in silver chloride crystals [2] as well as in multiphase materials mainly with cubic structures [6-9]. Similar observations have also been reported in hexagonal crystals, such as ice [10]. An observation of the prismatic punching behavior has, however not yet been reported in published literature for hexagonal SiC.

In this study, many foreign inclusions are observed in a physical vapor transport (PVT)-grown 4° off-axis 4H-SiC wafer, generating arrays of dislocations that present similar configurations as prismatic punched dislocation loops. A better understanding of the mechanisms of prismatic punching in 4H-SiC crystal through identification and characterization of the above dislocation arrays is the purpose of the reported work.

Experiment

Synchrotron X-ray topography (XRT) experiments were conducted on a PVT-grown 4° off-axis 6-inch 4H-SiC wafer. Transmission geometry topograph was recorded using synchrotron white beam X-ray in $11\bar{2}0$ reflection, Si-face as the beam exit surface. For grazing-incidence geometry using synchrotron monochromatic beam, $11\bar{2}8$ reflection topographs were recorded from the Si-face of the specimen at an energy of 8.99 keV, achieving an effective X-ray penetration depth range of 6-17 μm for BPDs [11]. $22\bar{4},16$ reflection topographs were recorded from the Si-face of the specimen at an energy of 18 keV for reaching a deeper effective X-ray penetration depth, which is approximately 30-40 μm for a screw type BPD. X-ray topography images were recorded on Agfa Structurix D3-SC films with approximately one μm resolution. The experiments were carried out at Beamline 1-BM of the Advanced Photon Source (APS) in Argonne National Laboratory (ANL).

The dislocation nature of defects observed topographically was confirmed by ray tracing simulations [12, 13]. The principle of ray tracing simulation is based on the orientation contrast mechanism [14], where the direction of local diffracted X-ray beams is calculated through the displacement field associated with the defect. The diffracted X-rays are then projected onto the recording plate. The distortion aroused by the presence of a dislocation within the crystal is revealed as dark or white contrast difference due to the superimposition or separation of diffracted X-rays resulting from the inhomogeneous intensity distributions. Ray tracing simulation presented in this study incorporated the effect of surface relaxation and photoelectric absorption for more precise contrast simulation [15-17].

Results and Discussion

Hexagonal-shaped foreign inclusion features (Fig. 1a, 1e) are observed optically over the inner region of the wafer. Such inclusions are characterized by synchrotron X-ray topography. While transmission geometry topography reveals information about defects contained in the whole sample volume by having X-ray beams incident onto one surface and exit from the other, grazing-incident topography uses reflection geometry that focuses on revealing defect configurations from the wafer surface down to the effective X-ray penetration depth exclusively [11, 18]. $11\bar{2}0$ reflection synchrotron white beam topograph recorded in transmission geometry revealed large dark strain contrast associated with each foreign inclusion feature observed optically (Fig. 1b). Whereas both $11\bar{2}8$ and $22\bar{4},16$ reflection synchrotron monochromatic beam topograph recorded in grazing-incidence geometry shows only part of the inclusions have correlated contrast (indicated by blue arrows in Fig. 1c, 1d). Such observations suggest foreign inclusions are located at different depths within crystal thickness. Enlarged grazing-incidence topograph indicates inclusions present white or dark contrast with frequent observation of associated dislocation arrays (Fig. 1f). This variation in inclusion contrast configuration is analyzed by ray tracing simulation. Simulated contrasts of an inclusion positioned at different depths below the crystal surface were calculated by applying equations describing the displacement field of a spherical inclusion [19]:

$$(r) = \varepsilon r \quad \text{when} \quad r < r_0 \tag{1}$$

$$u(r) = \frac{\varepsilon r_0^3}{r^2} \text{ when} \quad r > r_0 \tag{2}$$

where r is the distance from the center of the inclusion to the medium, r_0 is the size of the inclusion, and ε relates to the atomic volume difference between the inclusion and the lattice. Simulation results reveal a gradual change from the strong white dotted center surrounded by a dark ring to a dark dominated contrast as the inclusion embeds deeper into the crystal (Fig. 2).

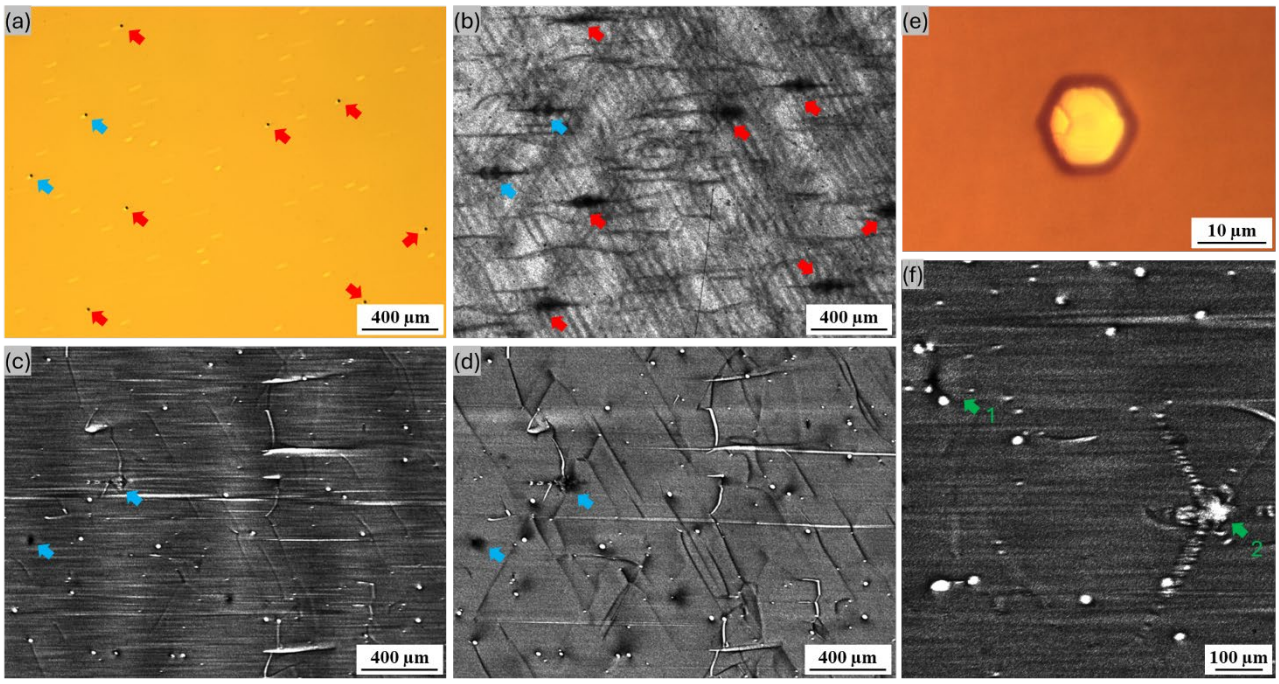

Fig. 1. Foreign inclusion features observed at the same region on a 4H-SiC wafer through (a) optical microscopy; (b) $11\bar{2}0$ transmission geometry X-ray topography; (c) $11\bar{2}8$ grazing-incidence geometry X-ray topography; (d) $22\bar{4}, 16$ grazing-incidence geometry X-ray topography. (e) Enlarged optical image of an inclusion feature. (f) Enlarged $11\bar{2}8$ X-ray topograph showing the dark (Arrow 1) and white (Arrow 2) contrast of inclusions and the expansion of dislocation arrays from the inclusion center.

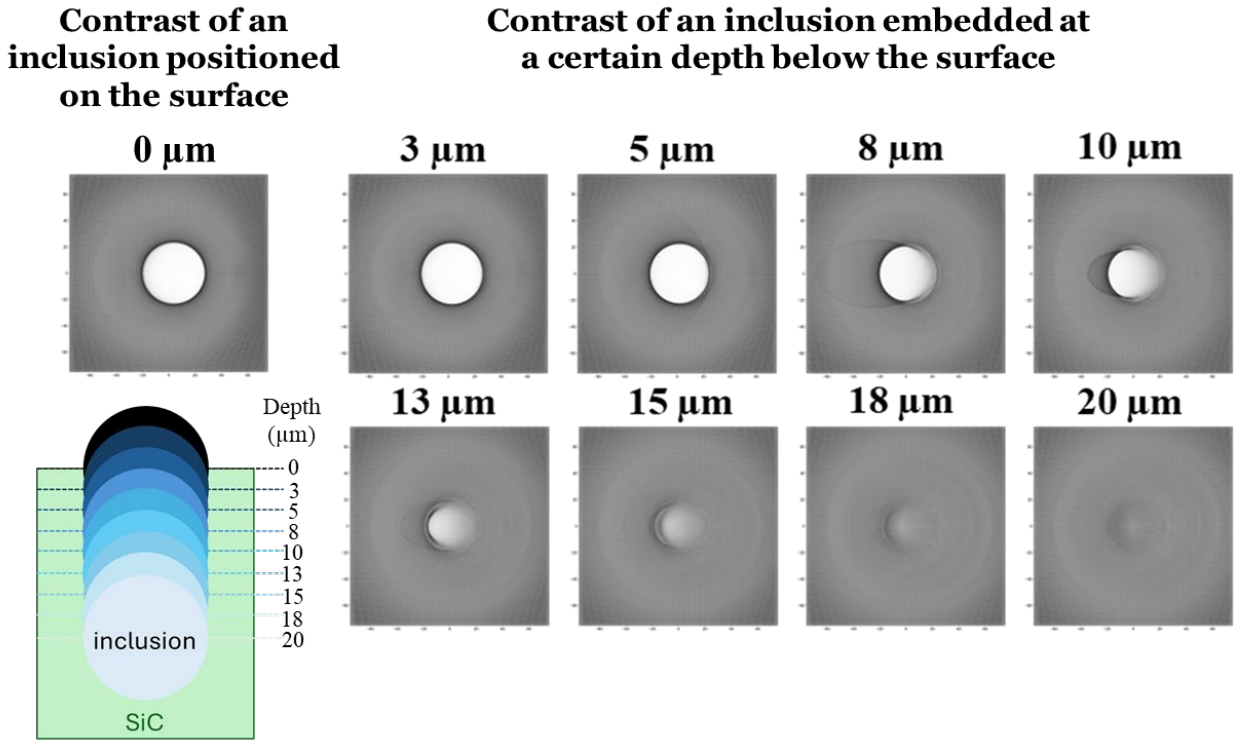

Fig. 2. Ray tracing simulation results of $11\bar{2}8$ reflection synchrotron monochromatic beam grazing-incidence topographic contrast of an inclusion located at the crystal surface and embedded at different depths below the surface. The location of the inclusion center with respect to the crystal is shown in the inset schematic diagram.

The prismatic punched dislocation loop is a well-known example of the nucleation of dislocations at stress concentrations. As shown in Fig. 3a, the indentation behavior of a foreign inclusion in 4H-SiC induces large shear stress, which activates prismatic punching and generates dislocation loops along six $\langle 11\bar{2}0\rangle$ directions. Each loop consists of two basal plane dislocation (BPD) segments lying on the basal plane and two threading edge dislocation (TED) segments along the growth axis. The Burgers vector of the dislocation is along $\langle 11\bar{2}0\rangle$ and is perpendicular to the prismatic loop. When a wafer is sliced from the boule, prismatic loops can be contained at varying depths within the wafer. As XRT is recorded on a wafer with reflection geometry, only volume from the sample surface to the X-ray effective penetration depth is imaged. This may contain only part of the prismatic punched dislocation loops within the imaged volume (Fig. 3b-d). Consequently, each set of prismatic punched dislocation loops aligned in the same direction may appear as arrays of TED pairs or BPDs on the topograph, depending on the intersection position of the dislocation loops relative to the wafer surface.

If the wafer is sliced across the middle of the prismatic loops (Fig. 3b), only a section of the threading segments along the growth axis is contained within the reflection XRT imaged volume, and prismatic loops will appear as pairs of opposite-signed TEDs (Fig. 4a). This is observed on grazing-incident topographs in both $11\bar{2}8$ and $22\bar{4},16$ reflections with different penetration depths as the example shown in Fig. 4b and Fig. 4c, where small paired dotted contrasts with symmetric or asymmetric configuration are generating from the inclusion center. Ray tracing simulation is conducted to simulate the contrasts of opposite-signed TED pairs along six $\langle 11\bar{2}0\rangle$ directions. Results indicate a symmetric configuration of opposite-signed TED arrays along horizontal $\pm[11\bar{2}0]$ directions (Fig. 4f, 4g) as both TEDs in the pair are with the same size and white contrast, whereas the inclined opposite-signed TED arrays in $\pm[2\bar{1}\bar{1}0]$ (fig. 4d, 4e) and $\pm[1\bar{2}10]$ (Fig. 4h, 4i) present asymmetric contrast with one larger white contrast TED and one smaller dark contrast TED in a pair. Such contrast configurations correlate well with actual topographic observations, thus verifying the composition of dislocation arrays associated with the inclusion.

If the wafer is sliced in a location where the reflection XRT imaged volume contains only the upper section of prismatic punched dislocation loops (Fig. 3c), dislocation segments along the basal plane as well as a short segment of threading-oriented dislocation on each side can be imaged (Fig. 5a). This corresponds to grazing-incidence topographic observation of BPD arrays generating from an inclusion if the effective X-ray penetration depth can only reach the dislocation segment on the basal plane (Fig. 5b). With a reflection that can focus deeper into the depth, two TEDs connecting a BPD in the arrays might be observable (Fig. 5c).

Finally, for wafer slicing position that intersects the lower portion of prismatic punched dislocation loops (Fig. 3d), grazing-incidence XRT can reveal prismatic loops as arrays of opposite-signed TED pairs, the visibility of BPD segment connecting two TEDs in a pair is determined by the effective X-ray penetration depth (Fig. 6a). As Fig. 6b shows, $11\bar{2}8$ reflection XRT captured the generation of dotted contrast arrays from an inclusion, which corresponds to the configuration of opposite-signed TEDs as previously discussed. However, $22\bar{4},16$ reflection XRT of the same region is recorded with a deeper penetration depth, which clearly reveals this array presents linear contrast corresponding to a BPD connecting two TEDs in a pair (Fig. 6c).

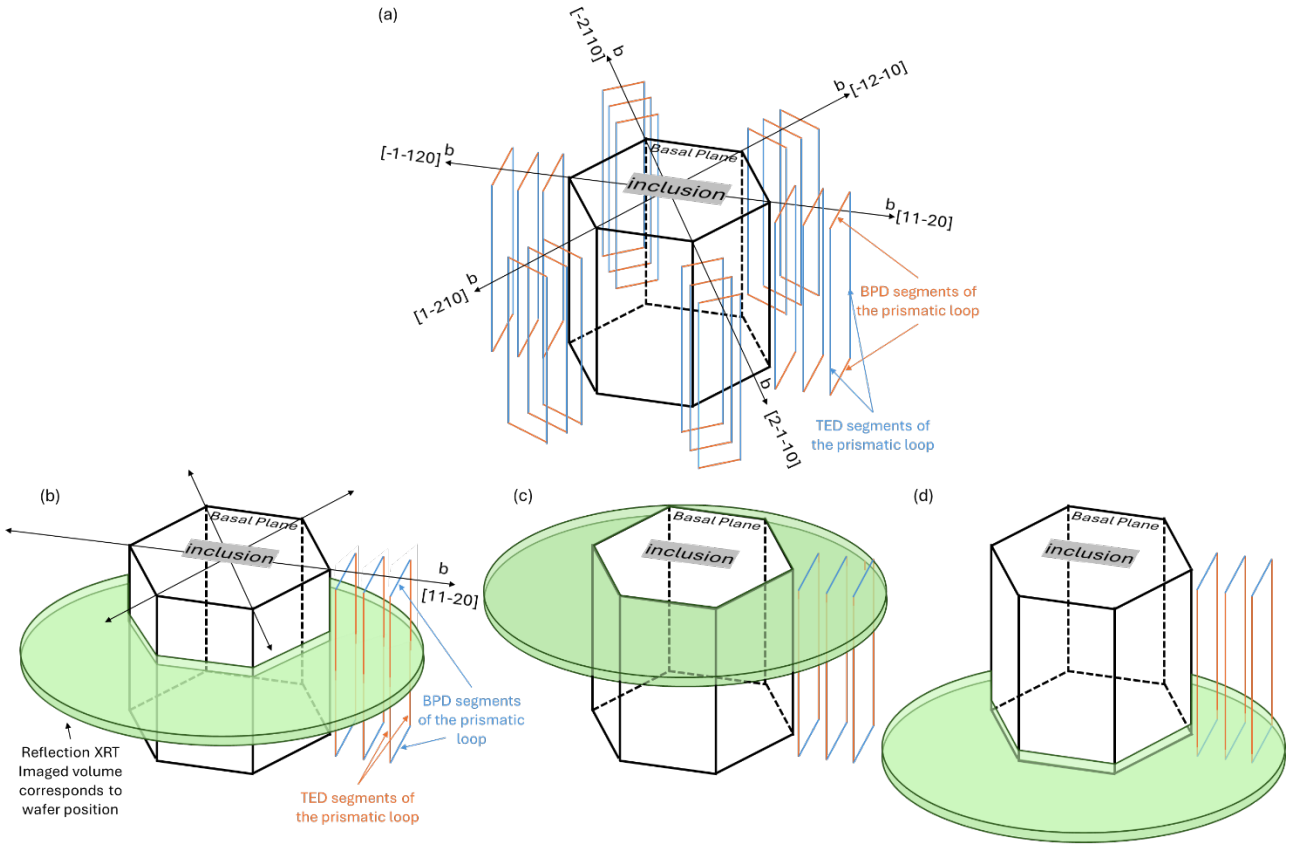

Fig. 3. Schematic diagrams showing (a) prismatic punched dislocation loops generating from an inclusion in 4H-SiC along six $\langle 11\bar{2}0 \rangle$ directions, each loop consists of two BPD segments lying on the basal plane and two TED segments along the growth axis; (b-d) the intersecting position of one set of prismatic loops and the imaged volume of a reflection geometry X-ray topograph corresponding to the wafer surface position down the effective X-ray penetration depth at (b) across the middle of dislocation loops; (c) across the upper part of dislocation loops; (d) across the lower section of dislocation loops.

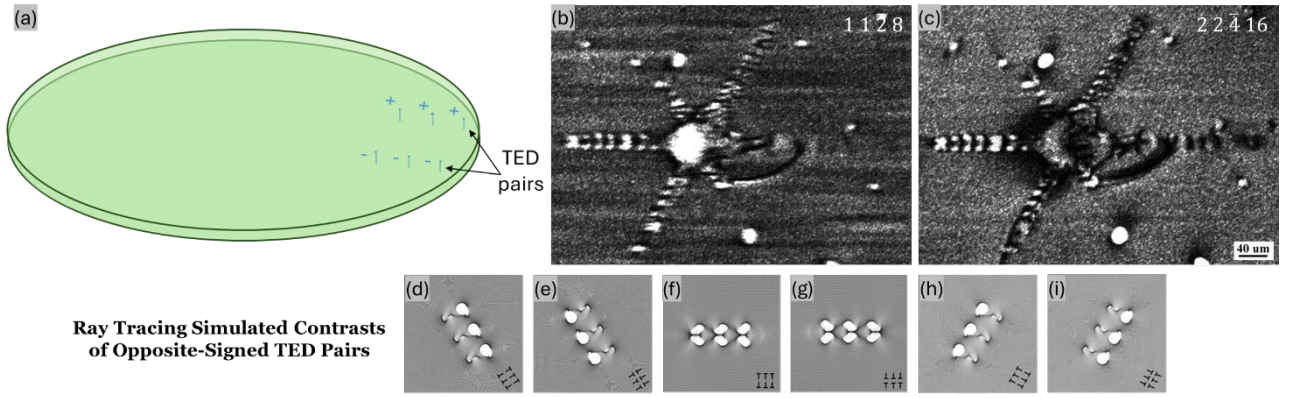

Fig. 4. (a) Schematic diagram showing a set of prismatic punched dislocation loops with their two threading segments along the *c*-axis contained in the reflection XRT imaged volume. Grazing-incidence synchrotron XRT presents corresponding contrasts of arrays of opposite-signed TED pairs in both (b) $11\bar{2}8$, and (c) $22\bar{4}$, 16 reflections. Such dislocation configurations are verified by (d-i) ray tracing simulated contrasts of opposite-signed TED pairs along six $\langle 11\bar{2}0 \rangle$ directions.

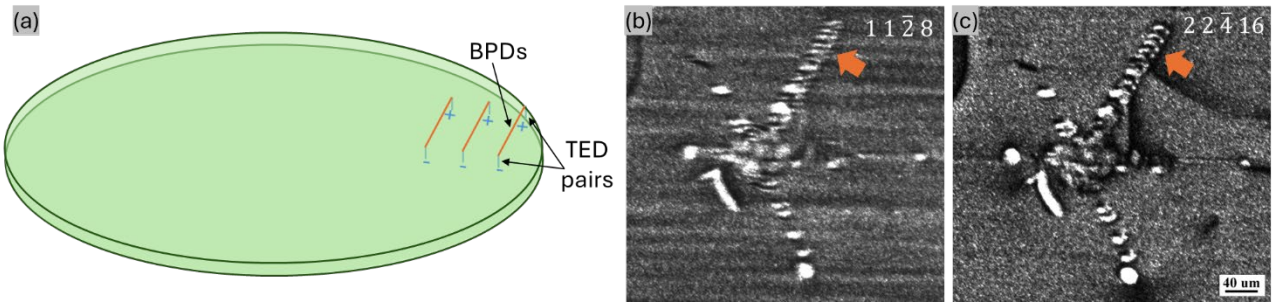

Fig. 5. (a) Schematic diagram showing a set of prismatic punched dislocation loops with their dislocation segment lying on the basal plane and two threading segments attached on each end contained in the reflection XRT imaged volume. Grazing-incidence synchrotron XRT presents corresponding contrasts of arrays of (a) BPDs in $11\bar{2}8$ reflection with shallower effective X-ray penetration depth; (c) opposite-signed TED pairs in $22\bar{4}, 16$ reflection with deeper penetration depth.

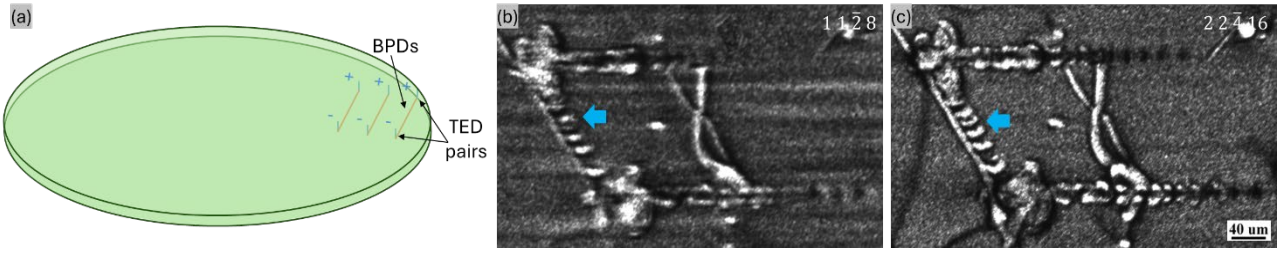

Fig. 6. (a) Schematic diagram showing a set of prismatic punched dislocation loops with their two short threading segments and the basal plane dislocation segment connecting in between contained in the reflection XRT imaged volume. Grazing-incidence synchrotron XRT presents corresponding contrasts of arrays of (a) TED pairs in $11\bar{2}8$ reflection with shallower effective X-ray penetration depth; (c) TED pairs connected by BPDs in $22\bar{4}, 16$ reflection with deeper penetration depth.

Since dislocation arrays expanding from an inclusion center present a similar contrast configuration as prismatic punched dislocation loops [2], stress induced by the presence of foreign inclusions within 4H-SiC bulk crystal is estimated to evaluate the possibility of prismatic loop generation. The difference in thermomechanical properties between the foreign inclusion material and the host crystal can result in shear stress arising as the crystal is cooled from the growth temperature, which can reach approximately 2400 °C during bulk SiC growth in the PVT method [20]. The brittle-to-ductile transition temperature of SiC is roughly 1050 °C [21], below which the material undergoes cleavage fracture with no plastic deformation. Within this temperature range, ΔT, the thermal expansion coefficients of the foreign inclusion material [22] and 4H-SiC along a-axis [23] are 6.42×10^{-6} °C^{-1} and 5.06×10^{-6} °C^{-1}, respectively. Assuming the inclusion is infinitely stiff, the effective thermal misfit strain ε in the 4H-SiC matrix due to the difference between the coefficients of thermal expansion ΔCTE of these two materials can be calculated as [24]:

$$\varepsilon = \Delta CTE \cdot \Delta T \tag{3}$$

Finally, the magnitude of shear stress τ induced by the presence of this foreign inclusion can be estimated according to the following equation [25]:

$$\tau = 3\varepsilon G \tag{4}$$

where G is the shear modulus of 4H-SiC. Literature indicates the shear modulus of 4H-SiC at 1800 K within the range between the brittle-to-ductile to the maximum growth temperature is 175.2 GPa [26], which yields a corresponding shear stress of 0.965 GPa due to the presence of a foreign inclusion. Since dislocation nucleation at appreciable rates occurs only for stresses approaching the theoretical

strength of perfect crystals [27], and the high-temperature strength of SiC at a comparable temperature level of 1773 K is 0.5 GPa [28], the estimated shear stress induced by this inclusion is then found sufficient for the generation of dislocations.

Summary

Prismatic punched dislocation loops are observed to be associated with inclusions on a PVT-grown 4H-SiC substrate wafer. Synchrotron X-ray topography in transmission geometry reveals inclusions are located at different depths within the crystal. The corresponding prismatic punched dislocation loops present contrast as arrays of opposite-signed TED pairs or BPDs along the $\langle 11\bar{2}0 \rangle$ directions on grazing-incidence synchrotron XRT. This contrast configuration variation depends on the intersecting position of prismatic loops and reflection XRT imaged volume corresponding to the wafer surface. Ray tracing simulation is conducted on contrasts of inclusion located at a depth of 0-20μm from the crystal surface, as well as on arrays of opposite-signed TED pairs. Such simulated contrasts present an excellent correlation with actual topographic observations, which further confirmed the generation of prismatic punched dislocation loops from foreign inclusions in 4H-SiC. Such prismatic loops are generated due to the indentation behavior of foreign inclusions that have a strong contrast of thermomechanical properties compared to SiC crystal, which induces large shear stress estimated at 0.965 GPa.

Acknowledgment

Work supported by and samples provided by SK siltron css. The research used resources of the Advanced Photon Source (Beamline 1-BM), a U.S. DOE Office of Science User Facility operated for the DOE Office of Science by Argonne National Laboratory under Contract No. DE-AC02-06CH11357. The Joint Photon Sciences Institute at SBU provided partial support for travel and subsistence at the Advanced Photon Source.

References

[1] F. Seitz, Prismatic Dislocations and Prismatic Punching in Crystals, Phys. Rev. 79 (1950) 723-724.

[2] D.A. Jones, J.W. Mitchell, Observations on helical dislocations in crystals of silver chloride, Philos. Mag.-J. Theor. Exp. Appl. Phys 3 (1958) p. 1-7.

[3] L.M. Brown, G.R. Woolhouse, The loss of coherency of precipitates and the generation of dislocations, Philos. Mag.-J. Theor. Exp. Appl. Phys 21 (1970) 329-345.

[4] M.F. Ashby, L. Johnson, On the generation of dislocations at misfitting particles in a ductile matrix, Philos. Mag.-J. Theor. Exp. Appl. Phys 20 (1969) 1009-1022.

[5] G.C. Weatherly, Loss of coherency of growing particles by the prismatic punching of dislocation loops, Philos. Mag.-J. Theor. Exp. Appl. Phys. 17 (1968) 791-799.

[6] Y. Flom, R.J. Arsenault, Deformation of SiC/Al Composites. JOM 38 (1986) 31-34.

[7] M. Wada, J. Suzuki, Characterization of Te Precipitates in CdTe Crystals, Jpn. J. Appl. Phys. 27 (1988) L972.

[8] A. Giannattasio, A., S. Senkader, R.J. Falster, P.R. Wilshaw, The role of prismatic dislocation loops in the generation of glide dislocations in Cz-silicon, Comput. Mater. Sci. 30 (2004) 131-136.

[9] H. Yu, A.C.F. Cocks, E. Tarleton, Formation of prismatic dislocation loops during unloading in nanoindentation, Scr. Mater. 189 (2020) 112-116.

[10] W.W. Webb, C.E. Hayes, Dislocations and plastic deformation of ice, Philos. Mag.-J. Theor. Exp. Appl. Phys. 16 (1967) 909-925.

[11] Q.Y. Cheng, H.Y. Peng, S.S. Hu, Z.Y. Chen, Y. Liu, B. Raghothamachar, M. Dudley, Ray-Tracing Simulation Analysis of Effective Penetration Depths on Grazing Incidence Synchrotron X-Ray Topographic Images of Basal Plane Dislocations in 4H-SiC Wafers, Mater. Sci. Forum 1062 (2022) 366-370.

[12] X.R. Huang, M. Dudley, W.M. Vetter, W. Huang, W. Si, C.H. Carter Jr, Superscrew dislocation contrast on synchrotron white-beam topographs: an accurate description of the direct dislocation image, J. Appl. Crystallogr. 32 (1999) 516-524.

[13] X.R. Huang, M. Dudley, W.M. Vetter, W. Huang, S. Wang, C.H. Carter Jr, Contrast Mechanism in Superscrew Dislocation Images on Synchrotron Back-Reflection Topographs, MRS Proceedings 524 (1998) 71.

[14] M. Dudley, X.R. Huang, W. Huang, Assessment of orientation and extinction contrast contributions to the direct dislocation image, J. Phys. D Appl. Phys. 32 (1999) A139.

[15] F. Fujie, H. Peng, T. Ailihumaer, B. Raghothamachar, M. Dudley, S. Harada, M. Tagawa, T. Ujihara, Synchrotron X-ray topographic image contrast variation of screw-type basal plane dislocations located at different depths below the crystal surface in 4H-SiC, Acta Mater. 208 (2021) 116746.

[16] H. Peng, T. Ailihumaer, F. Fujie, Z. Chen, B. Raghothamachar, M. Dudley, Influence of surface relaxation on the contrast of threading edge dislocations in synchrotron X-ray topographs under the condition of g . b = 0 and g . b x l = 0, J. Appl. Crystallogr. 54 (2021) 439-443.

[17] T. Ailihumaer, H. Peng, F. Fujie, B. Raghothamachar, M. Dudley, S. Harada, T. Ujihara, Surface relaxation and photoelectric absorption effects on synchrotron X-ray topographic images of dislocations lying on the basal plane in off-axis 4H-SiC crystals, Mater. Sci. Eng. B 271 (2021) 115281.

[18] Q.Y. Cheng, H.Y. Peng, Z.Y. Chen, S. Hu, Y. Liu, B. Raghothamachar, M. Dudley, Effective Penetration Depth Investigation for Frank Type Dislocation (Deflected TSDs/TMDs) on Grazing Incidence Synchrotron X-Ray Topographs of 4H-SiC Wafers. Defect and Diffusion Forum 426 (2023) 57-64.

[19] N.F. Mott, F.R.N. Nabarro, An attempt to estimate the degree of precipitation hardening, with a simple model, Proc. Phys. Soc. 52 (1940) 86.

[20] P.J. Wellmann, Review of SiC crystal growth technology, Semicond. Sci. Technol. 33 (2018) 103001.

[21] P. Pirouz, M. Zhang, J.L. Demenet, H.M. Hobgood, Transition from brittleness to ductility in SiC, J. Phys. Condens. Matter 14 (2002) 12929.

[22] A.G. Worthing, Physical Properties of Well Seasoned Mo and Ta as a Function of Temperature, Phys. Rev. 28 (1926) 1331-1331.

[23] Z. Li, R.C. Bradt, Thermal expansion of the hexagonal (4H) polytype of SiC, J. Appl. Phys. 60 (1986) 612-614.

[24] R.J. Arsenault, N. Shi, Dislocation generation due to differences between the coefficients of thermal expansion, Mater. Sci. Eng. 81 (1986) 175-187.

[25] D. Hull, D.J. Bacon, Chapter 8 - Origin and Multiplication of Dislocations, in: D. Hull, D.J. Bacon (Eds.), Introduction to Dislocations (Fifth Edition), Butterworth-Heinemann, Oxford, 2011, pp. 157-169.

[26] W.W. Xu, F. Xia, L. Chen, M. Wu, T. Gang, Y. Huang, High-temperature mechanical and thermodynamic properties of silicon carbide polytypes, J. Alloys Compd. 768 (2018) 722-732.

[27] J.P. Hirth, J. Lothe, Nucleation of Glide Loops, in: Theory of dislocations (2nd edition), John Wiley & Sons, Inc., New York, 1982, pp. 757-760.

[28] T. Kinoshita, S. Munekawa, S.I. Tanaka, Effect of grain boundary segregation on high-temperature strength of hot-pressed silicon carbide, Acta Mater. 45 (1997) 801-809.